RSC Advances

RSC Publishing

PAPER

Fluorine doped Fe_2O_3 nanostructures by a one-pot plasma-assisted strategy†

Cite this: *RSC Adv.*, 2013, **3**, 23762

G. Carraro,[a] A. Gasparotto,[a] C. Maccato,[a] E. Bontempi,[b] O. I. Lebedev,[c] S. Turner,[d] C. Sada,[e] L. E. Depero,[b] G. Van Tendeloo[d] and D. Barreca*[f]

Received 19th July 2013
Accepted 30th September 2013

DOI: 10.1039/c3ra43775b

www.rsc.org/advances

The present work reports on the synthesis of fluorine doped Fe_2O_3 nanomaterials by a single-step plasma enhanced-chemical vapor deposition (PE-CVD) strategy. In particular, $Fe(hfa)_2TMEDA$ (hfa = 1,1,1,5,5,5-hexafluoro-2,4-pentanedionate; TMEDA = *N*,*N*,*N*′,*N*′-tetramethylethylenediamine) was used as molecular source for both Fe and F in Ar/O_2 plasmas. The structure, morphology and chemical composition of the synthesized nanosystems were thoroughly analyzed by two-dimensional X-ray diffraction (XRD^2), field emission-scanning electron microscopy (FE-SEM), X-ray photoelectron spectroscopy (XPS), secondary ion mass spectrometry (SIMS) and transmission electron microscopy (TEM). A suitable choice of processing parameters enabled the selective formation of α-Fe_2O_3 nanomaterials, characterized by an homogeneous F doping, even at 100 °C. Interestingly, a simultaneous control of the system nanoscale organization and fluorine content could be achieved by varying the sole growth temperature. The tailored properties of the resulting materials can be favourably exploited for several technological applications, ranging from photocatalysis, to photoelectrochemical cells and gas sensing.

1. Introduction

Over the last decade, Fe_2O_3 has undoubtedly been one of the most investigated metal oxides, due to its abundance, non-toxicity and multi-functional properties.[1–7] In particular, nanoscale Fe_2O_3 systems hold significant promise for magnetic, electrochemical and photocatalytic applications.[8–13] Among the various iron(III) oxide polymorphs, α-Fe_2O_3 (hematite), the most stable one, is an attractive candidate for photocatalytic and photoelectrochemical water splitting promoted by solar radiation, due to its suitable band gap ($E_g \approx 2.2$ eV), chemical stability and low cost.[7,13–20] Nevertheless, α-Fe_2O_3 materials suffer from some disadvantages – such as high resistivity and fast recombination of photogenerated electrons/holes – which, in spite of several efforts, are far from being completely overcome.[2,5,11,14–16,18,21] To this regard, the ability to develop and process iron oxide-based systems with controlled nano-organization plays a key role for the fabrication of advanced nanodevices.[1,11,12,15,17,18] So far, several preparation strategies have been adopted for the synthesis of Fe_2O_3 nanosystems, such as hydrothermal approaches,[5,12,22] ballistic deposition,[3,20] sol–gel,[1] spray pyrolysis,[6,19] electrochemical routes,[17] atomic layer deposition[14] and chemical vapor deposition (CVD).[8–10,16,23] Along with the preparation route, further degrees of freedom to control Fe_2O_3 nanosystem properties are offered by its doping with suitable elements.[4,18] To date, several examples regarding the introduction of cationic dopants into hematite are available in the literature,[5,6,13,20,22,24] whereas the use of anionic dopants, such as fluorine, deserves further attention. As a matter of fact, F introduction in metal oxides can boost various beneficial effects, favorably affecting the material functional performances due to the concurrence of different phenomena.[25,26] In particular, the passivation of surface defects by fluorine can prevent the detrimental recombination of photogenerated electrons and holes, resulting in a higher charge carrier lifetime. Furthermore, F doping of oxide matrices might increase both the system electrical conductivity and absorption coefficient. The latter phenomenon, in turn, produces an improved light harvesting, of great importance for photoactivated applications. Last but not least, the substitution of O by F increases the Lewis acidity of iron centers, due to the electron withdrawing effect exerted by fluorine, enhancing thus the system catalytic activity.[25–30] Yet, in spite of these advantageous effects, F-doping of iron oxide photocatalysts has never been reported in the literature up to date.

Among the various approaches, PE-CVD has been shown to be a powerful synthetic tool for the control of material structure, morphology and composition.[7,16,25,31,32] Besides providing an

[a]*Department of Chemistry, Padova University and INSTM, 35131 Padova, Italy*
[b]*Chemistry for Technologies Laboratory, Brescia University and INSTM, 25123 Brescia, Italy*
[c]*Laboratoire CRISMAT, UMR 6508, CNRS-ENSICAEN, 14050 Caen Cedex 4, France*
[d]*EMAT, Antwerp University, 2020 Antwerpen, Belgium*
[e]*Department of Physics and Astronomy, Padova University, 35131 Padova, Italy*
[f]*CNR-IENI and INSTM, Department of Chemistry, Padova University, 35131 Padova, Italy. E-mail: davide.barreca@unipd.it; Tel: +39 049 8275170*

† Electronic supplementary information (ESI) available: Data on surface and in-depth XPS analyses of the obtained nanosystems. See DOI: 10.1039/c3ra43775b

inherent flexibility for the low-temperature growth of nanostructures with unique features, the use of non-equilibrium cold plasmas offers attractive possibilities for an *in situ* doping of the growing systems, due to the generation of fluorinated radicals in the plasma environment.[26] In particular, in this work we propose an amenable approach for the *in situ* synthesis and simultaneous F doping of hematite, involving the PE-CVD of α-Fe_2O_3 from $Fe(hfa)_2TMEDA$ in Ar/O_2 plasmas at 100–400 °C. Under these conditions, the adopted compound acts as a "single-source" precursor for both Fe and F, allowing to conveniently avoid the use of corrosive and/or toxic reactants (such as CF_4, F_2, NH_4F,…) and to prevent thermal stress/cracking phenomena occurring at higher temperatures.[33] Relevant results concerning the system chemico-physical features show that the obtained iron oxide materials present a controlled nano-organization, as well as a fluorine content directly dependent on the adopted growth temperature.

2. Experimental

2.1. Synthesis

The iron(II) molecular precursor $Fe(hfa)_2TMEDA$ was synthesized following a recently reported literature procedure.[34,35] Si(100) substrates (1.5×1.5 cm^2) were purchased from MEMC® (Merano, Italy). Prior to deposition, the substrates were cleaned by iterative dipping in a sulphonic detergent solution, deionized water and isopropylic alcohol, and finally dried under an Ar flow.

Growth experiments were carried out in Ar/O_2 plasmas (flow rates = 15 and 20 sccm), respectively, using a custom-built two-electrode radio frequency (RF, ν = 13.56 MHz) PE-CVD apparatus[36] (interelectrode distance = 6 cm). After preliminary optimization experiments, the total pressure, deposition time and RF-power were kept constant at 1.0 mbar, 60 min and 10 W, respectively. $Fe(hfa)_2TMEDA$, introduced in an external glass vessel, was vaporized at 65 °C by means of an oil bath, and its vapors were transported into the reaction chamber by an Ar flow (rate = 60 sccm). Gas lines were heated to 140 °C to prevent detrimental precursor condensation phenomena. Basing on preliminary experiments, four different deposition temperatures (100, 200, 300 and 400 °C) were adopted.

2.2. Characterization

XRD^2 images were collected by a Dymax-RAPID X-ray micro-diffractometer with a cylindrical imaging plate detector, that allows data acquisition in the 2θ ranges 0–160° (horizontally) and −45 to +45° (vertically) using CuKα radiation. Measurements were performed in reflection mode, adopting a collimator diameter of 300 μm and an exposure time of 30 min for each XRD^2 pattern.

FE-SEM micrographs were acquired using a Zeiss SUPRA 40VP instrument, at a primary beam acceleration voltage of 10 kV.

XPS analyses were performed on a Perkin-Elmer Φ 5600ci spectrometer, using a non-monochromatized AlKα excitation source ($h\nu$ = 1486.6 eV), at working pressures lower than 10^{-8} mbar. Binding energy (BE, standard deviation = ±0.2 eV) shifts were corrected for charging assigning a value of 284.8 eV to the adventitious C1s signal. Ar^+ sputtering was carried out at 3.0 kV with an Ar partial pressure of 5×10^{-8} mbar. Peak fitting was performed by a least-squares procedure, adopting Gaussian–Lorentzian peak shapes. The atomic percentages (at.%) were calculated by peak integration using standard PHI V5.4A sensitivity factors.

SIMS measurements were carried out by means of a Cameca IMS 4f spectrometer adopting a 14.5 keV Cs^+ primary beam (current = 20 nA), by negative secondary ion detection and electron gun charge compensation. Measurements were performed in high mass resolution configuration to avoid mass interference artefacts.

Samples for plane-view (pv) and cross-sectional (cs) TEM analyses were thinned down to electron transparency by polishing and ion-milling in a Balzers ion mill, starting with a 8 kV beam until perforation, continuing with a 5 kV beam for thinning and a 2 kV beam for final polishing. Conventional TEM, electron diffraction (ED) and high resolution (HR)-TEM analyses were performed using a Tecnai G2 30 UT microscope with a 0.17 nm point resolution, operated at 300 kV.

3. Results and discussion

In order to attain an insight into the system microstructure, with particular attention to the possible co-presence of various Fe_2O_3 polymorphs, XRD^2 experiments were carried out (Fig. 1).

At the lowest deposition temperature (100 °C), no appreciable diffraction peaks could be detected, due to the reduced system crystallinity. In a different way, for temperatures between 200 and 400 °C, the recorded XRD^2 images demonstrated the selective growth of pure α-Fe_2O_3. In particular, at 200 °C peaks located at $2\theta = 35.6°$ and 63.7°, related to (110) and (300) α-Fe_2O_3 (hematite, rhombohedral) reflections, were observed. Upon further increasing the growth temperature, patterns were characterized by the appearance of additional reflections at 2θ = 24.1° (012), 33.1° (104), 40.8° (113), 49.4° (024), 54.0° (116), 57.7° (018) and 62.3° (214).[37] As a general observation, at 300 °C the higher relative intensity of the (110) peak suggested the occurrence of a preferred orientation along this direction. This is confirmed by the corresponding XRD^2 image, showing that Debye rings intensities are not homogeneously distributed along the rings.[38]

Interestingly, the high (110)/(104) intensity ratio means that the Fe basal planes are perpendicular to the substrate. Since the conductivity parallel to the basal plane is higher than the one along the perpendicular direction, this can result in improved functional performances, especially in photoelectrochemical applications.[20]

As already anticipated, one of the main goals of the present work is the doping of iron(III) oxide with fluorine. In this regard, the analysis of the surface and in-depth system composition as a function of the synthesis conditions was accomplished by the complementary use of XPS and SIMS. The chemical composition of the prepared systems has been preliminarily investigated by XPS survey scans (Fig. S1, ESI†), showing the presence of Fe, O and F, along with the occurrence of C contamination.

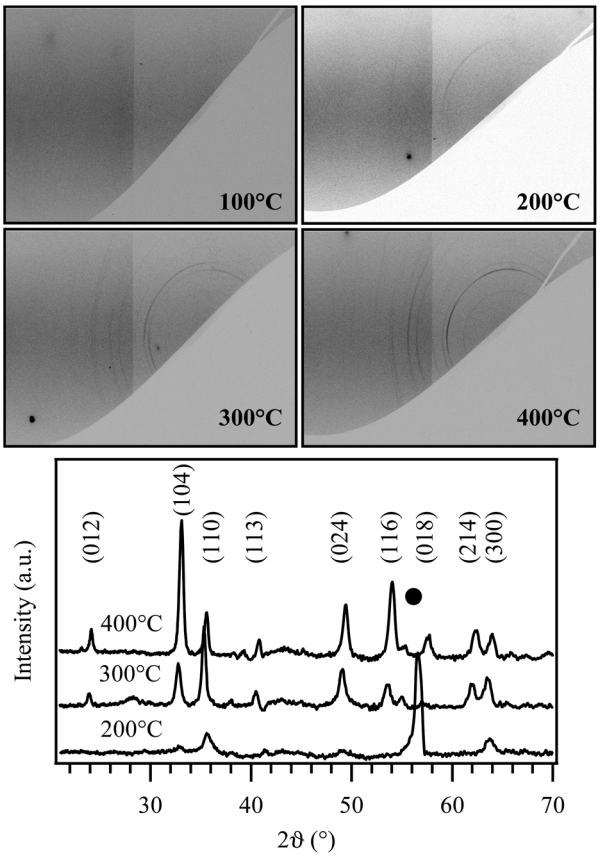

Fig. 1 XRD[2] maps and integrated XRD spectra for α-Fe_2O_3 nanosystems deposited at various temperatures. The substrate peak is marked with ●.

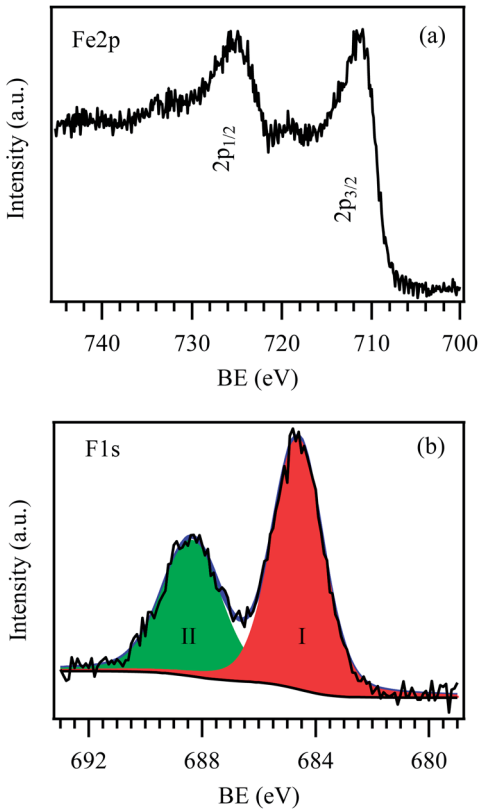

Fig. 2 Core-level Fe2p (a) and F1s (b) surface peaks for an α-Fe_2O_3 specimen grown at 200 °C.

The disappearance of carbon peaks to noise level after ~10 min of Ar^+ erosion evidenced the high purity of the obtained systems. The progressive intensity decrease of the F1s peak for higher deposition temperatures suggests the possibility of tailoring the fluorine doping level as a function of the adopted conditions (see below). Fig. 2a displays the surface Fe2p signal for a specimen grown at 200 °C. For all the analyzed systems, the Fe2p peak position [BE($Fe2p_{3/2}$) = 711.3 eV; spin–orbit separation = 13.8 eV] and the low intensity of shake-up satellites were in good agreement with the presence of iron(III) oxide, free from other Fe-containing species (see also Fig. S2, ESI†).[8,10,11,23,39] Regarding oxygen, the O1s peak (Fig. S3, ESI†) was characterized by the occurrence of two main contributions at BE = 530.0 eV, due to lattice oxygen in α-Fe_2O_3, and 531.8 eV, ascribed to chemisorbed hydroxyl groups.[8,11,22,23,39] In order to get detailed information on the content and nature of fluorinated species incorporated in the samples, particular attention was devoted to the analysis of the F1s photopeak (see Fig. 2b and S2, ESI†). As exemplified by Fig. 2b, this signal could be fitted by means of two different components, located at 684.7 (I) and 688.5 eV (II), respectively. The first band was attributed to the incorporation of fluorine into the iron(III) oxide lattice, resulting in the formation of Fe–F bonds. As a matter of fact, similar BE peak positions have been reported for other metal oxides doped with fluorine.[25,26,28,30] On the other hand, the second contribution at BE = 688.5 eV could be related to undecomposed CF_x precursor residuals.[7,25,26,30] It is worthwhile mentioning that this component completely disappeared after a few minutes of Ar^+ erosion, suggesting that the presence of CF_x moieties was confined to the outermost sample region. Conversely, component I, related to lattice fluorine, was retained even in the inner material layers (see Fig. S4, ESI†). Interestingly, the overall fluorine loading in the obtained Fe_2O_3 systems could be tailored as a function of the adopted deposition temperature, progressively decreasing from 12.0 at.% (at 100 °C) to 2.0 at.% (at 400 °C). A similar temperature dependence was observed for F doped Si and Co oxides synthesized by PE-CVD.[26,33]

To further investigate the material composition, in-depth SIMS measurements were carried out (Fig. 3). In general, all the samples presented a well-defined interface with the silicon substrate and an uniform composition throughout the entire thickness, as demonstrated by the O, Fe and F ionic yields. Remarkably, the almost parallel trend of fluorine with respect to iron signal pointed out to the achievement of a homogeneous Fe_2O_3 doping. To attain a relative estimation of fluorine concentration at different temperatures, the integral of F signal (I_F) as a function of depth was estimated for the various specimens throughout their thickness. I_F is in fact proportional to the areal density (expressed in at per cm^2), *i.e.* fluorine concentration for unit surface. The results, plotted as ln(I_F) in Fig. 3c, display a linear dependence on temperature, with a decay constant close to 50 ± 2 °C. This result highlights the

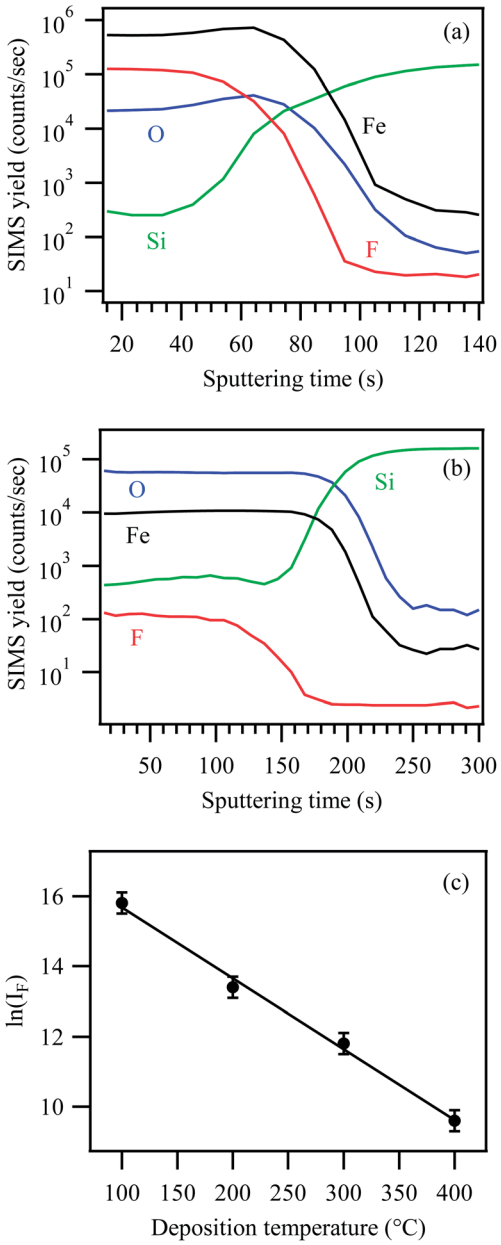

Fig. 3 (a and b) SIMS depth profile for samples deposited at 100 °C and 400 °C respectively. (c) Fluorine amount as a function of the deposition temperature.

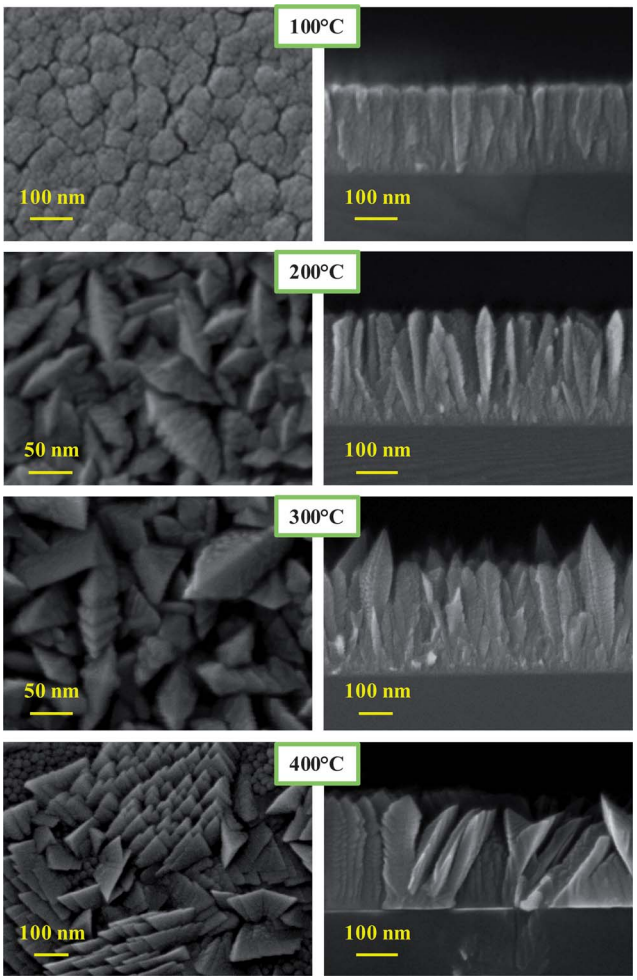

Fig. 4 FE-SEM pv (left) and cs (right) micrographs of Fe_2O_3 nanomaterials prepared at different deposition temperatures.

possibility of controlling F loading by tuning of the deposition temperature, an important issue to tailor the system properties affected by the dopant concentration.

Important preliminary clues on the system morphology as a function of the growth temperature were obtained by pv and cs FE-SEM analyses. Representative micrographs are displayed in Fig. 4. As a general observation, all specimens showed the presence of elongated nanostructures oriented almost perpendicularly to the substrate surface. In particular, the 100 °C sample was characterized by uniformly interconnected globular agglomerates (mean diameter = 70 ± 10 nm), resulting from the aggregation of vertically aligned columnar structures (length = 200 ± 10 nm). An increase of the substrate temperature to 200 °C produced a morphology evolution, resulting in the appearance of lamellar-like features with average width and length of 100 ± 30 and 350 ± 40 nm, respectively.

Whereas no dramatic difference in system nano-organization at 200 and 300 °C was observed, the specimen grown at 400 °C showed two different sets of nano-objects, namely rod-like structures (diameter = 20 ± 5 nm, length = 180 ± 20 nm) and lamellar structures (width = 30 ± 7 nm, length = 300 ± 20 nm). As a general observation, the nano-organization of the synthesized systems, suggesting a high active area, appears extremely promising in view of potential photocatalytic/sensing applications. In addition, nanostructures with reduced lateral size, like the present ones, offer the possibility of absorbing a significant light fraction while providing short charge carrier transport distances, minimizing thus recombination losses.[3,15,17] Typical growth rate values, calculated as the ratio between the overall specimen thickness and the deposition duration (60 min, see above) ranged between 3 and 6 nm min^{-1} in the adopted temperature range.

A further insight into the system nano-organization was gained by the use of advanced TEM analyses, which were carried out on representative samples grown at 300 and 400 °C. Selected

pv and cs bright field-TEM micrographs (Fig. 5) displayed the presence of columnar iron oxide structures, as already evidenced by FE-SEM analyses. ED patterns demonstrated that all grains exhibited the α-Fe_2O_3 (hematite) crystal structure,[37] in agreement with XRD results (see Fig. 1).

The specimen grown at 300 °C shows irregularly shaped, vertically aligned grains. The ED ring pattern taken from the cs sample confirmed its polycrystalline nature. Regarding the sample deposited at 400 °C, two regions with different columnar structures could be observed. The region indicated by I in both the pv and cs images displays α-Fe_2O_3 columns growing nearly perpendicular with respect to the substrate surface. In a different way, in region II the columns grew inclined with respect to the substrate. The electron diffraction ring pattern recorded in pv orientation again clearly confirmed the sample polycrystalline nature. A diffraction pattern taken from a single grain in cs indicated its single crystal nature, free from extended defects.

To achieve more detailed information, HR-TEM imaging was undertaken on representative grains of both samples. Fig. 6a provides a pv TEM image of the specimen grown at 300 °C. Four inter-grown α-Fe_2O_3 grains in this sample are displayed in low-magnification in (b), and in high resolution in (c). All four grains are imaged along the [100] zone axis and display a rounded, irregular morphology. A typical cs grain structure, showing near to *c*-oriented growth and imaged along the [$\bar{1}$10] zone axis orientation, is reported in Fig. 7. Again, the highly irregular shape of the α-Fe_2O_3 crystal columns is clearly confirmed. HR-TEM images of the sample synthesized at 400 °C (Fig. 8), acquired in cs, demonstrate that the columns in region I generally show a more rounded morphology (here with a near

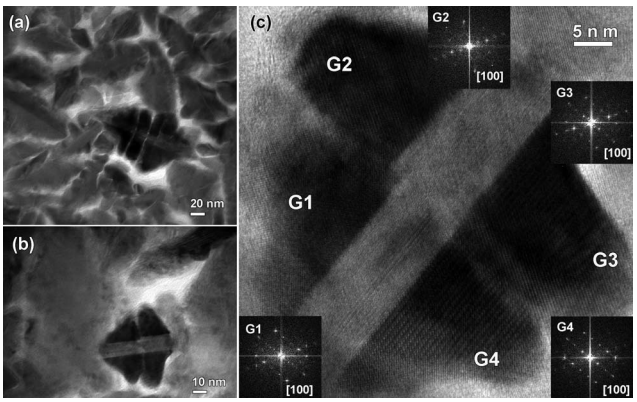

Fig. 6 Pv bright field-TEM (a and b) and HR-TEM (c) images of the Fe_2O_3 sample grown at 300 °C.

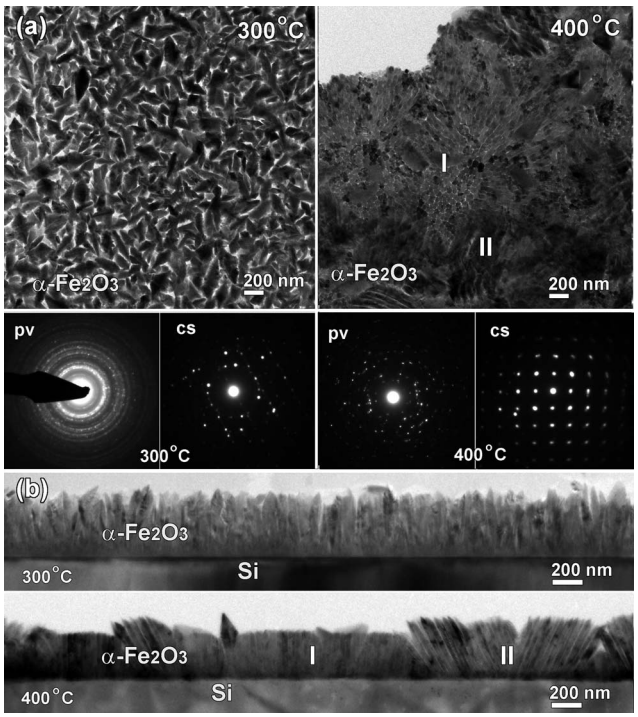

Fig. 5 (a) Pv bright field-TEM images of samples deposited at 300 and 400 °C. The corresponding ED patterns, all of which can be indexed to α-Fe_2O_3, are displayed for each of the two specimens. (b) Cs bright field-TEM images for both samples.

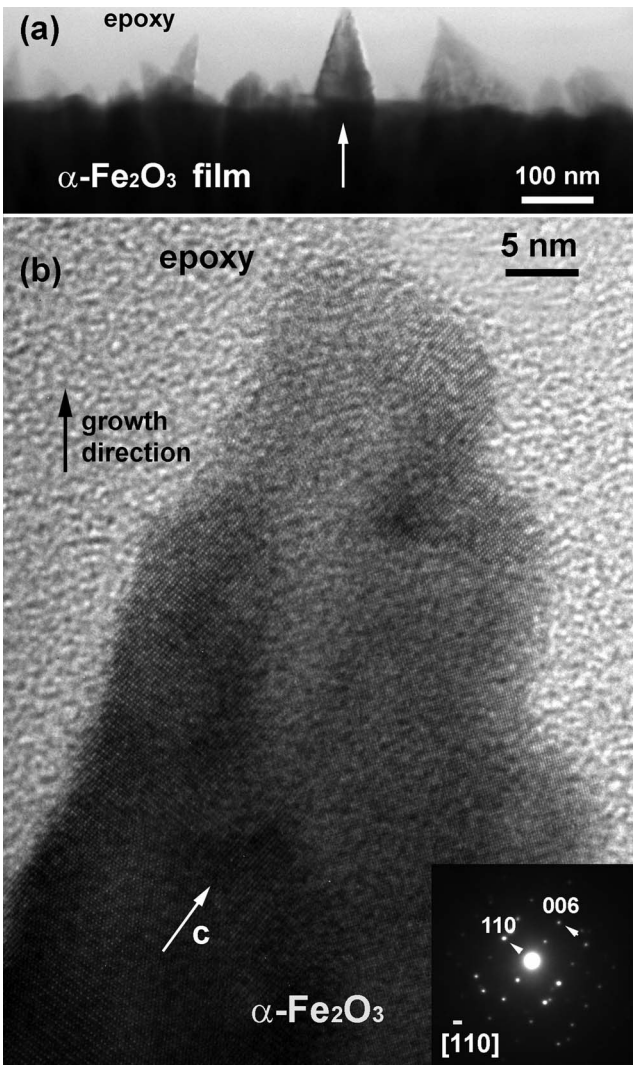

Fig. 7 Cs bright field-TEM (a) and HR-TEM (b) images of the Fe_2O_3 sample grown at 300 °C.

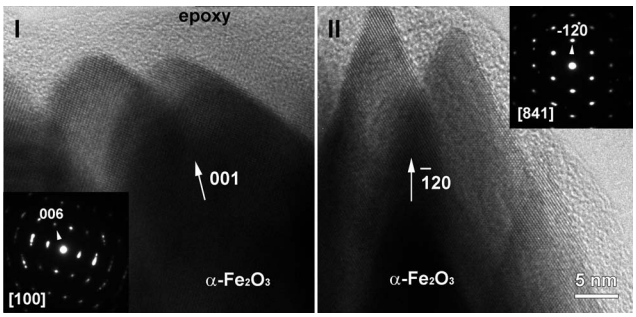

Fig. 8 Cs HR-TEM micrographs of typical α-Fe_2O_3 nanostructures in the nanodeposit obtained at 400 °C displaying a near [001]-oriented growth (region I) and a near [$\bar{1}$20] oriented growth (region II).

[001] growth direction), while the columns in region II evidenced a more sharply faceted saw-tooth shape (here with a near [$\bar{1}$20] growth direction).

4. Conclusions

This study was devoted to the development of a PE-CVD approach to fluorine doped iron(III) oxide nanosystems, using $Fe(hfa)_2TMEDA$ as a single-source molecular precursor for both iron and fluorine. The obtained materials, deposited at temperatures from 100 to 400 °C on Si(100) substrates under Ar/O_2 plasmas, showed the presence of the sole α-Fe_2O_3 (hematite) polymorph, and were composed of elongated nanostructures, with shapes ranging from lamellar to rod-like as a function of the processing parameters. Notably, a uniform in-depth fluorine doping could be successfully achieved, with an overall content tunable as a function of the adopted growth temperature. In addition, (HR)-TEM results clearly indicated that a change in deposition temperature had a significant influence on the morphology of the deposited materials.

The possibility to fabricate iron oxide nanostructures with a selected fluorine doping and a tunable nanoscale organization opens intriguing perspectives in various technological fields, such as solid-state gas sensing, photoassisted catalytic processes and photoelectrochemical cells. In particular, the fundamental information on the interrelations between the synthesis conditions and material characteristics, provided by the present work, is of crucial importance for the subsequent investigation and tailoring of functional behavior. To this regard, further efforts in the optimization of the target materials for their technological exploitation will be the subject of our future work, devoting also particular attention to the introduction of functional activators (such as Cu, Ag and Au-based nanoparticles) to enhance the performances of the obtained iron(III) oxide nanostructures.

Acknowledgements

The research leading to these results has received funding from the European Community's Seventh Framework Program (FP7/2007–2013) under grant agreement no. ENHANCE-238409. The authors also kindly acknowledge the financial support under the FP7 project SOLAROGENIX (NMP4-SL-2012-310333) as well as under Padova University ex-60% 2012 (no. 60A03-5517), PRAT 2010 (no. CPDA102579) and Regione Lombardia-INSTM ATLANTE projects. Thanks are also due to Dr D. Bekermann (Padova University, Padova, Italy) for synthetic assistance. S.T. acknowledges support from the Fund for Scientific Research Flanders (FWO).

Notes and references

1 L. Huo, Q. Li, H. Zhao, L. Yu, S. Gao and J. Zhao, *Sens. Actuators, B*, 2005, **107**, 915–920.
2 P. Tartaj, M. P. Morales, T. Gonzalez-Carreño, S. Veintemillas-Verdaguer and C. J. Serna, *Adv. Mater.*, 2011, **23**, 5243–5249.
3 N. T. Hahn, H. Ye, D. W. Flaherty, A. J. Bard and C. B. Mullins, *ACS Nano*, 2010, **4**, 1977–1986.
4 M. T. Mayer, Y. Lin, G. Yuan and D. Wang, *Acc. Chem. Res.*, 2013, **46**, 1558–1566.
5 V. M. Aroutiounian, V. M. Arakelyan, G. E. Shahnazaryan, H. R. Hovhannisyan, H. Wang and J. A. Turner, *Sol. Energy*, 2007, **81**, 1369–1376.
6 W. B. Ingler Jr and S. U. M. Khan, *Int. J. Hydrogen Energy*, 2005, **30**, 821–827.
7 G. Carraro, D. Barreca, D. Bekermann, T. Montini, A. Gasparotto, V. Gombac, C. Maccato and P. Fornasiero, *J. Nanosci. Nanotechnol.*, 2013, **13**, 4962–4968.
8 G. Carraro, D. Barreca, E. Comini, A. Gasparotto, C. Maccato, C. Sada and G. Sberveglieri, *CrystEngComm*, 2012, **14**, 6469–6476.
9 G. Carraro, D. Barreca, C. Maccato, E. Bontempi, L. E. Depero, C. de Julián Fernández and A. Caneschi, *CrystEngComm*, 2013, **15**, 1039–1042.
10 G. Carraro, D. Barreca, M. Cruz-Yusta, A. Gasparotto, C. Maccato, J. Morales, C. Sada and L. Sánchez, *ChemPhysChem*, 2012, **13**, 3798–3801.
11 X. Zhou, J. Lan, G. Liu, K. Deng, Y. Yang, G. Nie, J. Yu and L. Zhi, *Angew. Chem., Int. Ed.*, 2012, **51**, 178–182.
12 H. K. Mulmudi, N. Mathews, X. C. Dou, L. F. Xi, S. S. Pramana, Y. M. Lam and S. G. Mhaisalkar, *Electrochem. Commun.*, 2011, **13**, 951–954.
13 I. Cesar, K. Sivula, A. Kay, R. Zboril and M. Grätzel, *J. Phys. Chem. C*, 2009, **113**, 772–782.
14 B. Klahr, S. Gimenez, F. Fabregat-Santiago, T. Hamann and J. Bisquert, *J. Am. Chem. Soc.*, 2012, **134**, 4294–4302.
15 K. Sivula, F. Le Formal and M. Grätzel, *ChemSusChem*, 2011, **4**, 432–449.
16 A. P. Singh, A. Mettenbörger, P. Golus and S. Mathur, *Int. J. Hydrogen Energy*, 2012, **37**, 13983–13988.
17 C. S. Enache, Y. Q. Liang and R. van de Krol, *Thin Solid Films*, 2011, **520**, 1034–1040.
18 T. W. Hamann, *Dalton Trans.*, 2012, **41**, 7830–7834.
19 A. Duret and M. Grätzel, *J. Phys. Chem. B*, 2005, **109**, 17184–17191.

20 W. D. Chemelewski, N. T. Hahn and C. B. Mullins, *J. Phys. Chem. C*, 2012, **116**, 5255–5261.
21 D. K. Bora, A. Braun and E. C. Constable, *Energy Environ. Sci.*, 2013, **6**, 407–425.
22 H. G. Cha, J. Song, H. S. Kim, W. Shin, K. B. Yoon and Y. S. Kang, *Chem. Commun.*, 2011, **47**, 2441–2443.
23 G. Carraro, D. Barreca, A. Gasparotto and C. Maccato, *Surf. Sci. Spectra*, 2012, **19**, 1–12.
24 N. T. Hahn and C. B. Mullins, *Chem. Mater.*, 2010, **22**, 6474–6482.
25 A. Gasparotto, D. Barreca, D. Bekermann, A. Devi, R. A. Fischer, P. Fornasiero, V. Gombac, O. I. Lebedev, C. Maccato, T. Montini, G. Van Tendeloo and E. Tondello, *J. Am. Chem. Soc.*, 2011, **133**, 19362–19365.
26 D. Barreca, D. Bekermann, E. Comini, A. Devi, R. A. Fischer, A. Gasparotto, M. Gavagnin, C. Maccato, C. Sada, G. Sberveglieri and E. Tondello, *Sens. Actuators, B*, 2011, **160**, 79–86.
27 X. Chen, S. Shen, L. Guo and S. S. Mao, *Chem. Rev.*, 2010, **110**, 6503–6570.
28 H. Seo, L. R. Baker, A. Hervier, J. Kim, J. L. Whitten and G. A. Somorjai, *Nano Lett.*, 2010, **11**, 751–756.
29 B. Liu, M. Gu, X. Liu, S. Huang and C. Ni, *Appl. Phys. Lett.*, 2010, **97**, 122101–122103.
30 S. Sumitsawan, J. Cho, M. L. Sattler and R. B. Timmons, *Environ. Sci. Technol.*, 2011, **45**, 6970–6977.
31 A. Gasparotto, D. Barreca, D. Bekermann, A. Devi, R. A. Fischer, C. Maccato and E. Tondello, *J. Nanosci. Nanotechnol.*, 2011, **11**, 8206–8213.
32 J. Zheng, R. Yang, L. Xie, J. Qu, Y. Liu and X. Li, *Adv. Mater.*, 2010, **22**, 1451–1473.
33 W.-L. Lu, T.-W. Kuo, C.-H. Huang, N.-F. Wang, Y.-Z. Tsai, M. W. Wang, C.-I. Hung and M.-P. Houng, *Thin Solid Films*, 2011, **520**, 35–40.
34 D. Barreca, G. Carraro, A. Devi, E. Fois, A. Gasparotto, R. Seraglia, C. Maccato, C. Sada, G. Tabacchi, E. Tondello, A. Venzo and M. Winter, *Dalton Trans.*, 2012, **41**, 149–155.
35 D. Barreca, G. Carraro, A. Gasparotto, C. Maccato, R. Seraglia and G. Tabacchi, *Inorg. Chim. Acta*, 2012, **380**, 161–166.
36 D. Barreca, A. Gasparotto, E. Tondello, C. Sada, S. Polizzi and A. Benedetti, *Chem. Vap. Deposition*, 2003, **9**, 199–206.
37 Pattern no. 00-033-0664, JCPDS, 2000.
38 E. Bontempi and L. E. Depero, *Thin Solid Films*, 2004, **450**, 183–186.
39 J. F. Moulder, W. F. Stickle, P. E. Sobol and K. D. Bomben, *Handbook of X-ray photoelectron spectroscopy*, Perkin Elmer Corporation, Eden Prairie, MN, 1992.

